

Bluetooth Phased-array Aided Inertial Navigation Using Factor Graphs: Experimental Verification*

Glen Hjelmerud Mørkbak Sørensen* Torleiv H. Bryne*
 Kristoffer Gryte* Tor Arne Johansen*

* Department of Engineering Cybernetics, Norwegian University of Science and Technology (NTNU) NO-7491 Trondheim, Norway
 (corresponding author e-mail: glen.h.m.sorensen@ntnu.no).

Abstract: Phased-array Bluetooth systems have emerged as a low-cost alternative for performing aided inertial navigation in GNSS-denied use cases such as warehouse logistics, drone landings, and autonomous docking. Basing a navigation system off of commercial-off-the-shelf components may reduce the barrier of entry for phased-array radio navigation systems, albeit at the cost of significantly noisier measurements and relatively short feasible range. In this paper, we compare robust estimation strategies for a factor graph optimisation-based estimator using experimental data collected from multirotor drone flight. We evaluate performance in loss-of-GNSS scenarios when aided by Bluetooth angular measurements, as well as range or barometric pressure.

Keywords: Robust estimation, Angle of arrival measurements, Factor graph optimisation, GNSS-denied navigation, Bluetooth low energy (BLE)

1. INTRODUCTION

Global navigation satellite systems (GNSS) are ubiquitous in modern-day aided inertial navigation systems (INS). However, depending on the use case, GNSS may not be available at all (e.g., when indoors) or the availability of GNSS may be severely degraded due to natural or intentional interference (e.g., multipath in a dense urban area or signal jamming or spoofing). Consequently, GNSS-denied INS are necessary in these domains with examples including systems based on LiDAR (Brossard et al., 2022), vision (Lupton and Sukkarieh, 2012), and phased-array radio systems (PARS) (Okuhara et al., 2023).

Although most PARS-based navigation systems can be categorised as industry- or military-grade, *Bluetooth Low Energy* (BLE) PARS has emerged as a low-cost alternative based on commercial-off-the-shelf (COTS) components for aiding of e.g., fixed-wing UAV flight (Sollie et al., 2024). By basing a navigation system on COTS BLE components, the barrier of entry for employing such phased-array radio systems can be greatly reduced, albeit at the cost of a relatively short operating range and considerably noisier measurements. Furthermore, additional time synchronisation of measurements is necessary as a result of antenna switching and less stable oscillators (Sollie et al., 2022). Consequently, it is essential to employ robust estimation techniques to handle outliers.

In Sørensen et al. (2025), we presented an estimation scheme fusing PARS and inertial measurements based on factor graph optimisation (FGO), comparing performance against the industry-standard error-state Kalman filter (ESKF) in a simulation study. Outliers were handled with the natural test (NT), the Huber M-estimator, or the Tukey M-estimator (Gustafsson, 2010; Zhang, 1997) in the presence of simulated sensor faults. In this paper, we present the following contributions building on our previous publication:

- We apply our estimation framework on experimental data from multirotor drone flight, showcasing feasibility of BLE PARS-aided INS.
- We compare the performance of our FGO-based estimator on the $SE(3)$ matrix Lie group against a benchmark ESKF in handover scenarios where the drone goes from using Real-time kinematics (RTK)-GNSS aiding with position and compass measurements to (1) BLE PARS and RTK-GNSS range and (2) BLE PARS and barometric pressure.

RTK-based range measurements are used as an intermediary step since it allows us to experimentally verify the methods in the face of e.g., multipath. Integration of Bluetooth LE range from channel sounding (Nordic Semiconductor, 2025) is planned.

2. PRELIMINARIES

2.1 Notation and coordinate frames

Vectors and matrices are given in bold face, cursive lower-case v and uppercase letters A , respectively. R_a^b represents

* The work is supported by the Research Council of Norway through the project Phased-array radio systems for resilient localization and navigation of autonomous systems in GNSS-denied environments PARNAV (no. 338789).

This work has been submitted to IFAC for possible publication.

the rotation matrix between two coordinate frames, i.e., from frame $\{a\}$ to frame $\{b\}$. In this paper, four frames are considered: local North-East-Down navigation frame $\{n\}$, the BODY-frame $\{b\}$, the inertial measurement unit (IMU) sensor frame $\{s\}$, and the Bluetooth PARS radio frame $\{r\}$. E.g., \mathbf{p}_{rb}^n denotes the position measured in $\{b\}$ relative to $\{r\}$, decomposed in $\{n\}$. Estimates are expressed with a hat, e.g., \hat{x} is an estimate of x .

2.2 $SE(3)$ matrix Lie group theory

The $SE(3)$ matrix Lie group is defined as the set of poses $\mathbf{T} \in \mathbb{R}^{4 \times 4}$

$$SE(3) \triangleq \left\{ \mathbf{T} = \begin{bmatrix} \mathbf{R} & \mathbf{p} \\ \mathbf{0}_{1 \times 3} & 1 \end{bmatrix} \middle| \mathbf{R} \in SO(3), \mathbf{p} \in \mathbb{R}^3 \right\}, \quad (1)$$

with the corresponding *Lie algebra* $\mathfrak{se}(3)$ given by the set of matrices

$$\mathfrak{se}(3) \triangleq \left\{ \xi^\wedge = \begin{bmatrix} [\xi_o] \times & \xi_p \\ \mathbf{0}_{1 \times 3} & 0 \end{bmatrix} \middle| [\xi_o] \times \in \mathfrak{so}(3), \xi_p \in \mathbb{R}^3 \right\}, \quad (2)$$

where ξ_o is a small, local perturbation mapped to the Lie algebra using the hat operator $^\wedge$. The *exponential map* of the Lie group is subsequently defined using the matrix exponential: $\text{Exp}(\xi) \triangleq \exp(\xi^\wedge)$, and maps a matrix in the Lie algebra onto the Lie group itself. The reader is referred to Barfoot and Furgale (2014) for details.

3. BLUETOOTH LE DIRECTION FINDING

The angle-of-arrival (AoA) measurements from the Bluetooth PARS receiver are obtained using direction finding. This involves appending a *constant tone extension* (CTE) to each advertisement packet sent from the transmitter, which is subsequently sampled by the antennae at the receiver. The raw samples are then transformed into angular measurements (azimuth Ψ and elevation α), similar to the ones found in Gryte et al. (2019):

$$\mathbf{z}_{\text{PARS}}^r = \begin{bmatrix} \Psi^r \\ \alpha^r \end{bmatrix} = \begin{bmatrix} \arctan2(p_{rb,y}^r, p_{rb,x}^r) \\ \arctan2(-p_{rb,z}^r, \bar{p}) \end{bmatrix} + \boldsymbol{\varepsilon}, \quad (3)$$

where $\boldsymbol{\varepsilon}$ is zero-mean Gaussian noise and \bar{p} is the horizontal range of the measured position in $\{r\}$, i.e., the Euclidean distance between the horizontal components and the origin of $\{r\}$. This is the same model we used in Sørensen et al. (2025), with the notable exclusion of the range, which is not available with direction finding. The rotation matrix \mathbf{R}_r^n relating $\{r\}$ to $\{n\}$ needs to be estimated via rough calibration based on mounting or through some form of calibration algorithm using GNSS, as done in e.g., Okuhara et al. (2023). If the origin of $\{r\}$ differs from that of $\{n\}$, the lever arm $\mathbf{l}_{\text{PARS}}^n$ must also be accounted for, i.e., $\mathbf{p}_{rb}^n = \mathbf{R}_r^n \mathbf{p}_{rb}^r + \mathbf{l}_{\text{PARS}}^n$. The reader is referred to Nordic Semiconductor (2020) for details on the underlying direction finding technology and to Søllie et al. (2022) for details on the algorithm used for obtaining the angular measurements, as both are outside the scope of this paper.

4. INERTIAL NAVIGATION SYSTEM

This section presents the components of the FGO-based aided inertial navigation system. At its core, it is the same navigation system presented in Sørensen et al. (2025),

which is based on the iSAM2 fixed-lag smoother from the GTSAM C++ library developed by Dellaert et al. (2022).

The estimator maintains separate state- and covariance estimates of the pose, velocity, and IMU biases, i.e., $\hat{\mathbf{x}} \triangleq (\hat{\mathbf{T}}_b^n, \hat{\mathbf{v}}_{nb}^n, \hat{\mathbf{b}}^b) \in SE(3) \times \mathbb{R}^3 \times \mathbb{R}^6$, where $\hat{\mathbf{b}}^b \triangleq [\hat{\mathbf{b}}_{\text{acc}}^b, \hat{\mathbf{b}}_{\text{gyro}}^b]^\top$. The estimation itself is based on minimising

$$\hat{\mathbf{T}} = \arg \min_{\mathbf{T}} \|\mathbf{h}(\mathbf{T}) - \mathbf{z}\|_{\mathcal{P}}^2, \quad (4)$$

in the pose optimisation given in Ch. 6.2 in Dellaert and Kaess (2017) (and in equivalent expressions for the velocity and bias states). To solve the problem with respect to the local perturbation ξ , the problem is reformulated to

$$\hat{\xi} \approx \arg \min_{\xi} \|\mathbf{h}(\hat{\mathbf{T}}) + \mathbf{H}\xi - \mathbf{z}\|_{\mathcal{P}}^2, \quad (5)$$

where \mathbf{H} is the measurement Jacobian with respect to $\mathfrak{se}(3)$ (or velocity or bias) and \mathcal{P} is the given estimation error covariance. We first present the different measurement factors, before presenting the core navigation system.

4.1 On-manifold IMU preintegration factor

For on-manifold IMU preintegration, we use the model presented in Forster et al. (2015) to encode IMU measurements between two time steps i and j in an efficient manner:

$$\begin{aligned} \Delta \tilde{\mathbf{R}}_{ij} &= \mathbf{R}_i^\top \mathbf{R}_j \text{Exp}(\mathbf{w}_o) \\ \Delta \tilde{\mathbf{v}}_{ij} &= \mathbf{R}_i^\top (\mathbf{v}_j - \mathbf{v}_i - \mathbf{g} \Delta t_{ij}) + \mathbf{w}_v \\ \Delta \tilde{\mathbf{p}}_{ij} &= \mathbf{R}_i^\top (\mathbf{p}_j - \mathbf{p}_i - \mathbf{v}_i \Delta t_{ij} - \frac{1}{2} \mathbf{g} \Delta t_{ij}^2) + \mathbf{w}_p. \end{aligned} \quad (6)$$

Here, $\Delta \tilde{\mathbf{v}}_{ij}$ denotes the *preintegrated measurement* of the given state between the two time steps, Δt_{ij} is the time between the two given time steps, \mathbf{g} is the gravity vector, and \mathbf{w}_v is zero-mean Gaussian noise for angular velocity, acceleration, and the preintegration itself (from top to bottom). The implementation we use is GTSAM's internal on-manifold IMU preintegration factor, which is developed based on the above reference, as well as Lupton and Sukkarieh (2012); Carbone et al. (2014).

The pose and velocity estimates are propagated in between measurement updates using (6), whilst the bias estimates are updated whenever an optimisation is performed on the graph.

4.2 GNSS position and attitude factors

As a reference we employ the GNSS Factor (GPSFactor internally in GTSAM)

$$\mathbf{z}_{\text{RTK}}^n = \mathbf{p}_{nb}^n + \boldsymbol{\varepsilon}, \quad (7a)$$

$$\mathbf{h}_{\text{RTK}}(\hat{\mathbf{T}}) = \hat{\mathbf{p}}_{nb}^n, \quad (7b)$$

$$\mathbf{H}_{\text{RTK}} = \begin{bmatrix} \mathbf{0}_{3 \times 3} & \hat{\mathbf{R}}_b^n \end{bmatrix}, \quad (7c)$$

and a factor for GNSS compass

$$\mathbf{z}_{\text{comp}}^n = \mathbf{R}_b^n \mathbf{l}_{\text{RTK}}^b + \boldsymbol{\varepsilon}, \quad (8a)$$

$$\mathbf{h}_{\text{comp}}(\hat{\mathbf{T}}) = \hat{\mathbf{R}}_b^n \mathbf{l}_{\text{RTK}}^b, \quad (8b)$$

$$\mathbf{H}_{\text{comp}} = \begin{bmatrix} -\hat{\mathbf{R}}_b^n [\mathbf{l}_{\text{RTK}}^b] \times & \mathbf{0}_{3 \times 3} \end{bmatrix}, \quad (8c)$$

where $\mathbf{l}_{\text{RTK}}^b$ is the RTK baseline between the two GNSS antennae and $\boldsymbol{\varepsilon}$ is zero-mean Gaussian noise. These two factors are used before the handover to Bluetooth PARS-based aiding measurements to the navigation system.

4.3 Bluetooth factors

The Jacobians of the Bluetooth factors on $SE(3)$ are based on (3). Since BLE range is not present in the experimental data, we utilise range derived from the relative NED position from RTK in the interim

$$z_{\text{RTK range}}^r = \rho^r = \| \left(\hat{\mathbf{R}}_r^n \right)^\top (\mathbf{p}_{nb}^n - \mathbf{l}_{PARS}^n) + \boldsymbol{\varepsilon} \|_2, \quad (9)$$

and treat this as BLE PARS range as presented in our previous work. Thus, the Jacobians are given by

$$\mathbf{H}_\rho = \frac{1}{\| \hat{\mathbf{p}}_{rb}^r \|_2} (\hat{\mathbf{p}}_{rb}^r)^\top \mathbf{H}_p \quad (10a)$$

$$\mathbf{H}_\Psi = \frac{1}{\hat{p}_x^2 + \hat{p}_y^2} [-\hat{p}_y \ \hat{p}_x \ 0] \mathbf{H}_p \quad (10b)$$

$$\mathbf{H}_\alpha = \frac{1}{\| \hat{\mathbf{p}}_{rb}^r \|_2^2} \left[\begin{array}{cc} \frac{p_x p_z}{\sqrt{\hat{p}_x^2 + \hat{p}_y^2}} & \frac{p_y p_z}{\sqrt{\hat{p}_x^2 + \hat{p}_y^2}} \\ -\sqrt{\hat{p}_x^2 + \hat{p}_y^2} & 0 \end{array} \right] \mathbf{H}_p, \quad (10c)$$

where $\mathbf{H}_p = \left[\mathbf{0}_{3 \times 3} \left(\hat{\mathbf{R}}_r^n \right)^\top \hat{\mathbf{R}}_b^n \right]$ relates the position measured by the locator to $se(3)$. The Jacobians and corresponding factors were derived in Sørensen et al. (2025) and we refer to that paper for details. The difference between the two setups is that \mathbf{p}_{rb}^n is replaced with $\hat{\mathbf{R}}_r^n \mathbf{p}_{rb}^r$ in the derivations to get the Jacobians on $\{r\}$.

4.4 Barometric factor

We also use a barometer to provide vertical corrections with GTSAM internal barometric factor which is implemented based on the Earth atmosphere model found online (NASA Glenn Research Center, 2013):

$$z_{\text{baro}} = \frac{\frac{p_{\text{baro}}}{101.29}^{1/5.256} \cdot 288.08 - 288.14}{-0.00649} + \boldsymbol{\varepsilon} \quad (11a)$$

$$\hat{z} = [0 \ 0 \ -1] \hat{\mathbf{p}}_{nb}^n + \hat{b}_{\text{baro}} \quad (11b)$$

$$\mathbf{H}_{\text{baro}, SE(3)} = [\mathbf{0}_{1 \times 3} \ [0 \ 0 \ 1] \hat{\mathbf{R}}_b^n] \quad (11c)$$

$$\mathbf{H}_{\text{baro}, \text{baro}} = 1, \quad (11d)$$

where $\boldsymbol{\varepsilon}$ is zero-mean Gaussian noise and p_{baro} is the pressure measurement from the barometer given in kPa. Similarly to the IMU biases, \hat{b}_{baro} must be modelled and estimated, e.g., as a random walk or a constant.

4.5 Propagating the estimate and dealing with outliers

The INS uses the predicted state from the preintegrator between measurement updates. Whenever an aiding measurement is available, a factor representing the preintegrated IMU measurement since the last update is added to the factor graph alongside the aiding measurement factor(s). The fixed-lag smoother then calculates the updated estimate and resets the preintegrator with the updated IMU bias estimate.

Each factor will have an uncertainty associated with it, typically modelled as zero-mean Gaussian noise. In the implementation, the noise model is “wrapped” in a robust model representing one of two *M-estimators* in order to mitigate outliers. Initially proposed in Huber (1964), M-estimators are a group of estimators suitable for mitigating the effect of outliers without necessarily rejecting them outright. Here, they differ from the natural

test (Gustafsson, 2010, Ch. 7.6), which is a technique that rejects a measurement outright if the test statistic exceeds the given threshold.

In this study, we apply the *Tukey* and *Geman-McClure* M-estimators on the experimental multirotor data. They are described by their objective/cost functions $Q_\bullet(\tilde{z})$

$$Q_T(\tilde{z}) = \begin{cases} \frac{c^2}{6} (1 - [1 - (\tilde{z} - (\tilde{z}/c)^2)^3]), & \text{for } |\tilde{z}| \leq c \\ \frac{c^2}{6}, & \text{otherwise,} \end{cases} \quad (12)$$

$$Q_G(\tilde{z}) = \frac{1}{2} \frac{c^2 \tilde{z}^2}{c^2 + \tilde{z}^2}, \quad (13)$$

for Tukey (TK) and Geman-McClure (GM), respectively. c is the given estimator bound and \tilde{z} denotes the residual between the measurement and its predicted value (*innovation*). We note that the two estimators behave differently – Tukey caps large outliers at a constant max value if the residual exceeds the threshold, whereas Geman-McClure smooths the curve in a continuous fashion, suitable for real-time use. In our previous paper, we considered the Huber M-estimator alongside Tukey and found that the former’s inclusion of outliers no matter how large resulted in poorer performance which is why we omit it from this study. The reader is referred to Zhang (1997); Yang et al. (2026) for further details on the M-estimators.

5. EXPERIMENT SETUP

The multirotor drone flight experiment data were obtained from an experimental campaign at one of NTNU’s test sites in a field west of Trondheim. The drone and ground station are both equipped with a Raspberry Pi 4B, Nordic Semiconductor nRF52833 BLE devkit, and Sentsystems Sentiboard v1.3. The ground station BLE devkit is connected to a 12-element antenna array, whilst the drone is equipped with a STIM300 IMU, a barometric pressure sensor, and a uBlox dual RTK GNSS receiver. The drone runs a modified version of the DUNE robotic middleware (Pinto et al., 2013) and uses the Pixhawk Cube Orange autopilot with ArduCopter v4.6.0. The drone and ground station are shown in Fig. 1. After takeoff, the wooden frame was moved as to not obstruct line-of-sight between the drone-mounted transmitter and ground station receiver. During the experiment, the drone followed a preconfigured path given by the autopilot software. The relative NED position computed from the measurements is shown in Fig. 2.

The empirical update rates of the sensors used are approximately: 2000Hz for the IMU, 1Hz for RTK, 2Hz for barometer, and 16.6Hz for BLE PARS. In order to obtain range measurements for PARS, the RTK position measurements are interpolated at the IMU frequency and measurements that match BLE PARS timestamps are used to compute range for that given time.

The following pre-processing is performed:

- IMU specific force and angular velocity measurements are transformed from $\{s\}$ to $\{b\}$ using \mathbf{R}_s^b , which is roughly known.
- The raw IQ samples from Bluetooth are converted into angular measurements.

We compare the FGO-based estimation scheme with smoother lag set to $t_{\text{lag}} = 2$ s against a benchmark ESKF in



Fig. 1. Multirotor drone and ground station in the field. The Bluetooth antenna array (green) is mounted flat.

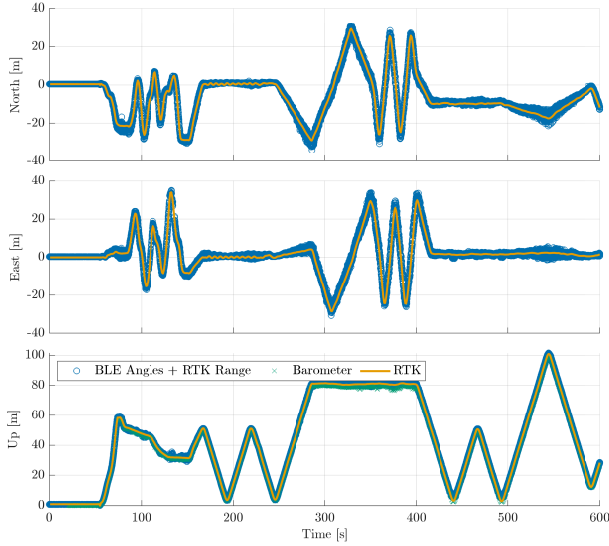


Fig. 2. NED position computed from measurements.

a handover scenario, where the drone switches from navigating aided by RTK position and compass measurements to aiding by Bluetooth angular measurements and either RTK-based range or barometric pressure measurements. In the latter case, the barometer measurements are used before handover to allow the barometer bias estimate to converge.

Outside of the nominal comparison (i.e., using BLE PARS measurements without any outlier rejection or mitigation) the following configurations are tested:

- ESKF + Outlier rejection with the NT with $k = 3.841$
- FGO + Tukey M-estimator with $c = 3.6851$
- FGO + Geman-McClure M-estimator with $c = 1$

The tuning of the different methods are kept as close to one another as possible. The interpolated position from RTK in $\{n\}$ at the frequency of the IMU is chosen as ground truth for position. We compare the roll and pitch estimates with the autopilot's own estimates, whilst the yaw computed from the dual GNSS receiver is chosen as yaw reference. We evaluate performance using the root mean square error (RMSE) of each substate, as well as the estimation error and corresponding 3σ -bounds.

We use the QUEST algorithm to obtain our initial estimate of the drone attitude whilst stationary, see Shuster and Oh (1981) for details. The GNSS compass is used for further stabilisation of the attitude before the handover, and is not used afterwards.

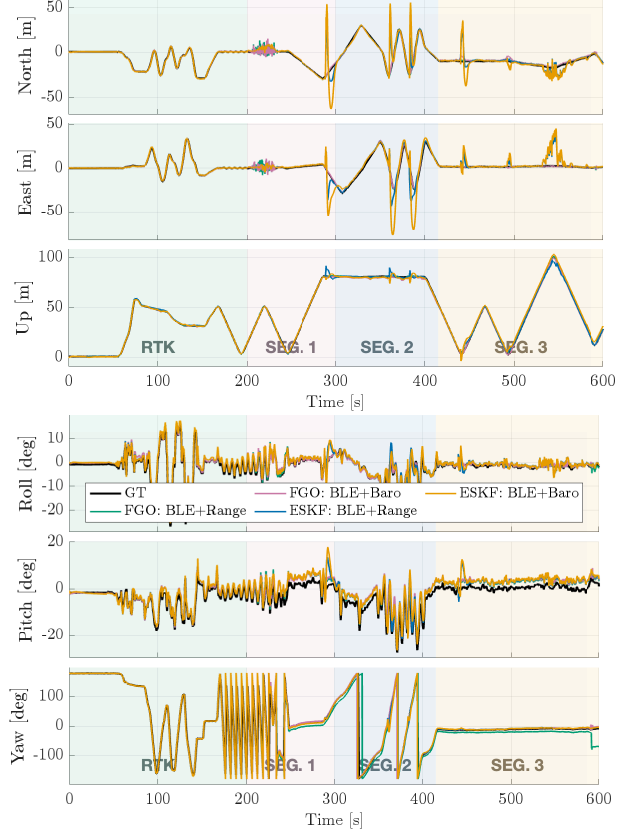


Fig. 3. Estimator performance without mitigation of BLE PARS outliers. Note the shaded sections roughly segmenting the data based on RTK/PARS and the manoeuvre performed during the given time interval.

6. RESULTS AND DISCUSSION

This section presents the performance of the ESKF and FGO-based estimators and discusses the findings. For comparison, the position and attitude estimates when the BLE measurements are used without any outlier mitigation/rejection are shown in Fig. 3. The data is roughly segmented based on the manoeuvre and whether we have switched from RTK, and we will refer to these segments as *segments* throughout this section. We highlight two problematic areas – one shortly after the set handover point in section 1 and one shortly after the 500s mark until the end of the run (section 4). In addition, we observe some spikes in the North-East position estimate in section 2, though these mostly affect the ESKF.

6.1 BLE angular measurements and RTK range

The estimation error for NED position and attitude in the handover case to BLE angular measurements and RTK range are shown in Tab. 1 and Fig. 4. We observe comparable performance across the board for position. The Down-position is consistently well-estimated, with the FGO configurations achieving equivalent or marginally better performance in all segments. We generally observe good estimation of the NE-error, albeit with a higher uncertainty for FGO with Tukey than the other configurations shortly after the handover. Given that this is one of the problematic areas, it is reasonable to assume that Tukey has set the influence of some of the measurements to

Table 1. RMSE BLE angular + RTK range.

		N [m]	E [m]	D [m]	ϕ [°]	θ [°]	ψ [°]
RTK	NT	0.391	0.454	0.416	1.168	1.197	23.132
	TK	0.344	0.312	0.238	1.251	1.193	23.076
	GM	0.344	0.312	0.238	1.251	1.193	23.076
SEG. 1	NT	1.548	1.478	0.512	0.850	2.981	41.853
	TK	0.917	0.696	0.287	0.808	3.130	41.791
	GM	0.844	0.574	0.288	0.835	3.117	41.786
SEG. 2	NT	0.921	1.639	0.409	0.688	2.909	19.840
	TK	0.821	1.641	0.411	0.705	3.040	19.235
	GM	0.842	1.670	0.410	0.701	3.012	19.797
SEG. 3	NT	0.819	0.347	0.717	0.590	3.114	2.307
	TK	0.883	0.401	0.652	0.492	3.038	2.356
	GM	0.883	0.583	0.665	0.541	3.044	1.584

Table 2. RMSE BLE angular + Barometer.

		N [m]	E [m]	D [m]	ϕ [°]	θ [°]	ψ [°]
RTK	NT	0.404	0.461	0.345	1.155	1.199	23.128
	TK	0.345	0.312	0.386	1.250	1.196	23.076
	GM	0.345	0.312	0.386	1.250	1.196	23.076
SEG. 1	NT	2.866	1.664	0.424	0.873	3.049	41.852
	TK	1.150	0.834	0.443	0.799	3.147	41.796
	GM	0.880	0.587	0.436	0.831	3.118	41.787
SEG. 2	NT	1.120	1.742	1.145	0.732	2.948	19.797
	TK	0.978	1.598	1.303	0.715	3.053	19.194
	GM	1.000	1.630	1.270	0.708	3.020	19.797
SEG. 3	NT	1.402	2.959	0.485	0.573	3.172	2.575
	TK	1.536	0.403	0.680	0.451	3.002	2.688
	GM	1.476	0.572	0.610	0.524	3.031	1.400

(near)-zero, so an increased uncertainty is to be expected. Similarly, when considering the benchmark ESKF, we observe some spikes in the NE-estimate in segment 1, likely due to measurements being rejected by the natural test, resulting in less available information during filter updates.

The rapid yaw changes in segment 1 are challenging for all configurations, resulting in several spikes in estimation error wrapping around $\pm 180^\circ$, resulting in a large RMSE. However, we note that even before RTK is lost, the estimator is struggling with this manoeuvre, which may indicate that e.g., the gyroscope bias is not properly estimated. By incorporating information from, e.g., magnetometer aiding or using multiple PARS antennas on the drone, this issue may be mitigated. The roll angle is well-estimated, but for pitch, we observe a bias between the autopilot's and our estimate after the handover. A possible explanation may be misalignment in specified mounting angles of the PARS antenna array or a delay/time synchronisation issue in the AoA measurements or artefacts from the AoA estimation.

6.2 BLE angular measurements and barometric pressure

The estimation results for position and attitude in the handover case to BLE angular measurements and barometric pressure are shown in Tab. 2 and Fig. 5. Performance is generally comparable to the first case, but we observe slightly greater position uncertainty overall, with the ESKF affected the most. These differences can also be seen in the relevant RMSE values. Given that the range measurements are received at the same rate as the BLE

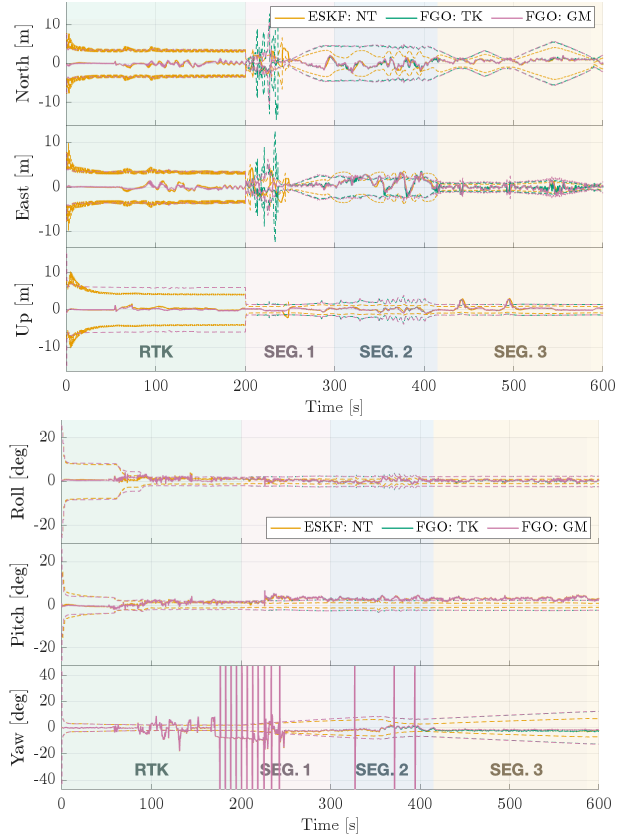


Fig. 4. Estimation error in handover from RTK to BLE angular measurements and RTK range. 3σ -bounds are given by dashed lines of the same colour.

measurements, whilst the barometer measurements are received at a rate of 2Hz, there will consequently be fewer measurements available. Furthermore, the updates will in general not be synchronised like those in the previous case. Together, this may explain some of the more notable fluctuations in the estimation error in this case.

7. CONCLUSION

The results demonstrate the feasibility of our Bluetooth PARS-aided FGO-based estimator for GNSS-denied navigation at short ranges. Position is well-estimated and erroneous data are handled better by the FGO-based navigation system configurations compared to equivalent based on the ESKF. Rapid yaw changes of the drone are challenging, but may be mitigated by, e.g., INS aiding from a magnetometer or by mounting multiple PARS antennas on the drone. The two M-estimators tested achieve comparable performance, with Tukey resulting in higher estimation uncertainty in the first segment.

Future work includes incorporating BLE range via channel sounding in order to make a fully-fledged Bluetooth-aided INS. Making use of a more sophisticated calibration method to determine the antenna orientation is also of particular interest, as this can make the system more suitable for use in real-time experiments down the line.

ACKNOWLEDGEMENTS

The authors would like to thank colleagues at NTNU: Johan Nicolas Suarez at the Department of Electronic

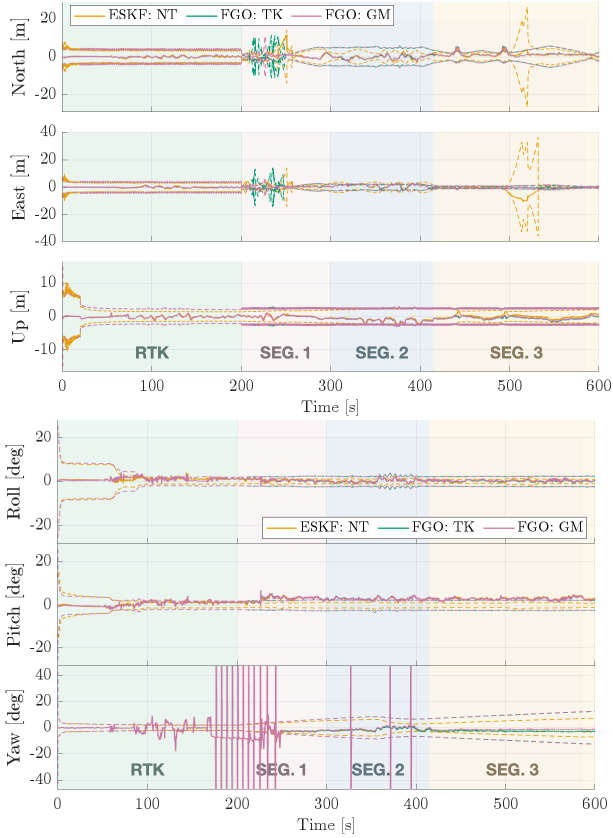


Fig. 5. Estimation error in handover from RTK to BLE angular measurements and barometric pressure. 3σ -bounds are given by dashed lines of the same colour.

Systems and Pål Kvaløy and Morten Einarsve at the Department of Engineering Cybernetics for their help in conducting field experiments with the multirotor drone. Johan Nicolas Suarez also participated in the post-processing and analysis work involved in converting the raw BLE PARS measurements into angular measurements.

REFERENCES

Barfoot, T.D. and Furgale, P.T. (2014). Associating Uncertainty With Three-Dimensional Poses for Use in Estimation Problems. *IEEE Trans. Robot.*, 30(3), 679–693.

Brossard, M., Barrau, A., Chauchat, P., and Bonnabel, S. (2022). Associating Uncertainty to Extended Poses for on Lie Group IMU Preintegration With Rotating Earth. *IEEE Trans. Robot.*, 38(2), 998–1015.

Carlone, L., Kira, Z., Beall, C., Indelman, V., and Dellaert, F. (2014). Eliminating conditionally independent sets in factor graphs: A unifying perspective based on smart factors. In *2014 IEEE Int. Conf. on Robotics and Automation (ICRA)*, 4290–4297. ISSN: 1050-4729.

Dellaert, F. and Kaess, M. (2017). Factor Graphs for Robot Perception. *Foundations and Trends in Robotics*, 6(1-2), 1–139.

Dellaert, F. et al. (2022). borglab/gtsam. URL <https://github.com/borglab/gtsam>.

Forster, C., Carlone, L., Dellaert, F., and Scaramuzza, D. (2015). IMU Preintegration on Manifold for Efficient Visual-Inertial Maximum-a-Posteriori Estimation. In *Robotics: Science and Systems XI*. Robotics: Science and Systems Foundation.

Gryte, K., Bryne, T.H., Albrektsen, S.M., and Johansen, T.A. (2019). Field Test Results of GNSS-denied Inertial Navigation aided by Phased-array Radio Systems for UAVs. In *2019 Int. Conf. on Unmanned Aircraft Systems (ICUAS)*, 1398–1406. IEEE, Atlanta, GA, USA.

Gustafsson, F. (2010). *Statistical sensor fusion*. Studentlitteratur, 3rd edition.

Huber, P.J. (1964). Robust Estimation of a Location Parameter. *The Annals of Mathematical Statistics*, 35(1), 73–101. Publisher: Institute of Mathematical Statistics.

Lupton, T. and Sukkarieh, S. (2012). Visual-Inertial-Aided Navigation for High-Dynamic Motion in Built Environments Without Initial Conditions. *IEEE Trans. Robot.*, 28(1), 61–76.

NASA Glenn Research Center (2013). Earth Atmosphere Model - Metric Units. URL <https://www.grc.nasa.gov/www/k-12/airplane/atmosmet.html>.

Nordic Semiconductor (2020). Bluetooth Direction Finding Whitepaper. URL https://docs.nordicsemi.com/bundle/nwp_036/page/WP/nwp_036/intro.html.

Nordic Semiconductor (2025). Bluetooth® Channel Sounding. URL <https://www.bluetooth.com/learn-about-bluetooth/feature-enhancements/channel-sounding/>.

Okuhara, M., Bryne, T.H., Gryte, K., and Johansen, T.A. (2023). Phased Array Radio Navigation System on UAVs: Real-Time Implementation of In-flight Calibration. *IFAC-PapersOnLine*, 56(2), 1152–1159.

Pinto, J., Dias, P.S., Martins, R., Fortuna, J., Marques, E., and Sousa, J. (2013). The LSTS toolchain for networked vehicle systems. In *2013 MTS/IEEE OCEANS - Bergen*, 1–9. IEEE, Bergen.

Shuster, M.D. and Oh, S.D. (1981). Three-axis attitude determination from vector observations. *Journal of Guidance and Control*, 4(1), 70–77. Publisher: American Institute of Aeronautics and Astronautics.

Sollie, M.L., Gryte, K., Bryne, T.H., and Johansen, T.A. (2024). Automatic Recovery of Fixed-Wing Unmanned Aerial Vehicle Using Bluetooth Angle-of-Arrival Navigation. In *2024 Int. Conf. on Unmanned Aircraft Systems (ICUAS)*, 390–397. ISSN: 2575-7296.

Sollie, M.L., Gryte, K., Bryne, T.H., and Johansen, T.A. (2022). Outdoor Navigation Using Bluetooth Angle-of-Arrival Measurements. *IEEE Access*, 10, 88012–88033.

Sørensen, G.H.M., Bryne, T.H., Gryte, K., Synnevåg, T., and Johansen, T.A. (2025). Robust phased-array radio system aided inertial navigation using factor graph optimisation. In *2025 European Control Conf. (ECC)*, 1787–1794. ISSN: 2996-8895.

Yang, H., Mangelson, J., Chang, Y., Shi, J., and Carlone, L. (2026). Robustness to incorrect data association and outliers. In L. Carlone, A. Kim, T. Barfoot, D. Cremers, and F. Dellaert (eds.), *SLAM Handbook. From Localization and Mapping to Spatial Intelligence*. Cambridge University Press.

Zhang, Z. (1997). Parameter Estimation Techniques: A Tutorial with Application to Conic Fitting. *Image and Vision Computing*, 15(1), 59–76.